AMERICAN METEOROLOGICAL SOCIETY
AMS Journals Online

Full Text View

Lagrangian Motion and Fluid Exchange in a Barotropic Meandering Jet

A. M. Rogerson

Woods Hole Oceanographic Institution, Woods Hole, Massachusetts

P. D. Miller

Stevens Institute of Technology, Hoboken, New Jersey

L. J. Pratt

Woods Hole Oceanographic Institution, Woods Hole, Massachusetts

C. K. R. T. Jones

Brown University, Providence, Rhode Island

ABSTRACT

Kinematic models predict that a coherent structure, such as a jet or an eddy, in an unsteady flow can exchange fluid with its surroundings. The authors consider the significance of this effect for a fully nonlinear, dynamically consistent, barotropic model of a meandering jet. The calculated volume transport associated with this fluid exchange is comparable to that of fluid crossing the Gulf Stream through the detachment of rings. Although the model is barotropic and idealized in other ways, the transport calculations suggest that this exchange mechanism may be important in lateral transport or potential vorticity budget analyses for the Gulf Stream and other oceanic jets. The numerically simulated meandering jet is obtained by allowing a small-amplitude unstable meander to grow until a saturated state occurs. The resulting flow is characterized by finite-amplitude meanders propagating with nearly constant speed, and the results clearly illustrate the stretching and stirring of fluid particles along the edges of the recirculation regions south of the meander crests and north of the troughs. The fluid exchange and resulting transport across boundaries separating regions of predominantly prograde, retrograde, and recirculating motion is quantified using a dynamical systems analysis. The geometrical structures that result from the analysis are shown to be closely correlated with regions of the flow that are susceptible to high potential vorticity

Options:
- Create Reference
- Email this Article
- Add to MyArchive
- Search AMS Glossary

Search CrossRef for:
- Articles Citing This Article

dissipation. Moreover, in a related study this analysis has been used to effectively predict the entrainment and detrainment of particles to and from the jet.

1. Introduction

It is well known that horizontal fluid exchange and mixing in the Gulf Stream and other oceanic jets can result from the detachment of rings and other spin-off eddies. More recently, attention has been focused on the prospect that exchange and stirring can occur due to the meandering motions of the stream in the absence of eddy detachments (Bower 1991; Bower and Lozier 1994). Support for this idea comes from models of wavy flows that have simple Eulerian time dependence but 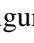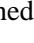very complicated Lagrangian motion. In simple models of meandering jets with periodic or quasiperiodic time dependence for example, the flow contains regions in which fluid blobs are continually stretched and stirred, resulting in chaotic Lagrangian motion. The fluid parcels that participate in this process are able to move across regime boundaries that separate regions of the flow exhibiting qualitatively different types of motion. The associated volume flux across such boundaries is called "chaotic transport" and it can be calculated using a method known as "lobe dynamics" (Wiggins 1992). As summarized below, many of the simple jet models for which this mechanism has been illustrated are kinematic or involve other restrictions, such as linearity.
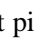
This paper has several aims. First, we describe the fluid motion and lobe dynamics in a meandering jet that is fully nonlinear and temporally aperiodic (and therefore one step closer to reality). The resulting lobe diagrams provide a new way of visualizing meandering flow fields and can be used to interpret drifter data (Lozier et al. 1997). Second, we suggest the importance for fluid exchange and mixing within the Gulf Stream and other meandering jets by calculating the dimensional transport and showing it to be comparable to transports caused by Gulf Stream rings. Also, we use the lobe calculations to identify regions of strong fluid filamentation and, through calculation of changes in potential vorticity along particle trajectories, we show these regions to be ones of high dissipation. Finally, we demonstrate by example the application of a potentially important dynamical systems analysis to model data that is aperiodic and available only over a finite time.
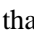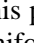
a. Background

A number of earlier studies have suggested the existence of chaotic fluid exchange in meandering jets. Many of these studies build on Bower's kinematic model of Lagrangian behavior in a jet with steadily propagating meanders (Bower 1991). For such a flow, the motion may be rendered steady by changing to a frame of reference translating with the meander phase speed. Figure 1 ⊙ shows a typical streamfunction pattern caused by a meander propagating at a speed within the velocity range of the eastward jet. In the frame of reference moving with the meander, regions containing three types of motion appear. Near the meandering centerline or core of the jet exists a prograde region (labeled $\mathcal{R}_1$) containing eastward streaming motion. Far away from the jet lie retrograde regions (labeled $\mathcal{R}_3$) containing westward streaming motion, and between the retrograde and prograde regions lie recirculations or "cat's eyes" (labeled $\mathcal{R}_2$). The recirculations are centered about the critical lines, defined as values of y at which the phase speed c equals the velocity $u(y)$ of the background jet. These recirculations should not be confused with the broader recirculation gyres known to exist north and south of the Gulf Stream. The points labeled p_1 and p_2 are hyperbolic stagnation points. The term "hyperbolic" implies pure straining motion, with fluid moving toward or away from p_1 or p_2 along "stable" and "unstable" directions, respectively, as indicated by the arrows in Fig. 1 ⊙. In this steady flow, the streamlines are pathlines and therefore the streamlines connecting the hyperbolic points to the north of the crests and to the south of the troughs are regime boundaries separating the prograde ($\mathcal{R}_1$), recirculation ($\mathcal{R}_2$), and retrograde ($\mathcal{R}_3$) regions. In Bower's model, no fluid exchange occurs across the bounding streamlines (the edges of the cat's eyes) and the Lagrangian motion is regular (nonchaotic).

When additional time dependence is added to the steadily propagating meander, it is no longer possible to render the flow steady by shifting reference frames. In the studies of Behringer et al. (1991), Samelson (1992), Meyers (1994), and Duan and Wiggins (1996) additional time dependence is included by superimposing meanders of different frequencies or by modulating the amplitude of the original meander. In all cases, chaotic exchange occurs across the regime boundaries and the stretching and folding associated with chaotic motion implies stirring in the vicinity of these boundaries. [Dutkiewicz et al. (1993) effected a similar result by adding a diffusive process.] This process is depicted in Fig. 2 ⊙ for a time-periodic meandering jet flow (from Miller et al. 1996). The Lagrangian motion of particles in the vicinity of the cat's eye is represented by a Poincaré map, which marks the locations of different particle trajectories at the end of each time period. The points p_1 and p_2 of Fig. 2 ⊙ are generalizations of the hyperbolic stagnation points of the steady flow. In the time-periodic case p_1 and p_2 mark periodic trajectories, that is, trajectories for which the fluid element in question passes the

same location at the end of each time period. Point p_1 is intersected by a solid curve $W^u(p_1)$ called an unstable manifold of p_1. In the absence of time dependence, $W^u(p_1)$ relaxes to the boundary separating the recirculating and prograde regions in the steady case (Fig. 1 ⊙). As in the steady case, we can define $W^u(p_1)$ as the collection of trajectories that diverge from p_1 (or, equivalently, approach p_1 as $t \rightarrow -\infty$). Any fluid element that initially lies on $W^u(p_1)$ must continue to lie along this curve after subsequent iterations of the map. Similarly, a continuous material segment initially lying along this curve will map to another material segment on the curve. The motion of material elements or contour segments along $W^u(p_1)$ follows the arrows marked in the figure. Note that p_1 has a stable manifold (also a solid curve in Fig. 2 ⊙), which defines the collection of all trajectories that approach p_1 as $t \rightarrow \infty$. The point p_2 has its own stable and unstable manifolds and the former, $W^s(p_2)$, is shown as a dashed line in Fig. 2 ⊙.

It is sometimes helpful to think of the stable and unstable manifolds as surfaces in the three-dimensional space (x, y, t). For example, one might picture the time axis as perpendicular to the (x, y) plane of Fig. 2 ⊙. Then the trajectories of all fluid elements, which initially lie on $W^u(p_1)$, form a material surface. Time slices of this surface yield curves like $W^u(p_1)$, and these curves are identical when the time slices are taken periodically. Visualizing the manifolds this way is also very helpful when the time dependence becomes aperiodic, in which case the time slices no longer replicate themselves exactly.

In the steady case $W^u(p_1)$ and $W^s(p_2)$ are identical, but this is no longer true in the periodic case. Instead, $W^u(p_1)$ and $W^s(p_2)$ are distinct curves that intersect each other at an infinite number of points (labeled q_0, $\tilde{q}_0$, q_1, $\tilde{q}_1$, etc., in Fig. 2 ⊙). Between successive intersection points are segments of the unstable and stable manifolds that delineate regions of fluid called lobes (labeled A_0, A_1, B_0, B_1, etc.). Since any point lying initially on a manifold must be mapped to another point on the same manifold, the intersection points must be mapped to other intersection points (say $\tilde{q}_{-1}$ to $\tilde{q}_0$ and q_{-1} to q_0) and material segments like $\tilde{q}_{-1}q_{-1}$ are mapped to, say, $\tilde{q}_0q_0$, and then to $\tilde{q}_1q_1$. It follows that the material contained in a particular lobe, say A_{-1}, is mapped into a different lobe, say A_0, then to A_1, and so on. (More complicated scenarios, such as movement from A_{-1} to A_1 to A_3 can also occur, but we assume this is not the case here.) Similarly, material from B_{-1} is mapped to B_0, then to B_1, and so on.

Two fundamentally important events occur as a result of this motion. First, fluid is transported from the prograde region $\mathcal{R}_1$ to the recirculating region (or cat's eye) $\mathcal{R}_2$, and vice versa. For example, the material in A_{-1} (which clearly lies outside $\mathcal{R}_2$) is eventually mapped to A_2 (which clearly lies inside). Similarly, the material in B_{-1} (which lies inside $\mathcal{R}_2$) is mapped to B_2 (which lies outside). The cat's eye may now be regarded as a region where the motion is *predominantly* recirculating but experiences exchanges with the prograde and retrograde regions. The second important event is that fluid entering $\mathcal{R}_2$ through the "A" lobes becomes stretched and folded, as suggested by the deformation of the solid dye patches shown in Fig. 2 ⊙. This process is due in part to the fact that there is an infinite number of intersection points between the stable and unstable manifolds and, consequently, they become densely packed in the neighborhood of the hyperbolic points. For example, the distance between $\tilde{q}_n$ and q_n, which is a measure of the width of lobe A_n decreases to zero as n increases. To conserve area, as required by mass conservation, the lobes must lengthen. This filamentation process tends to increase property gradients, eventually bringing diffusive processes into play.

The boundaries separating $\mathcal{R}_1$ and $\mathcal{R}_2$ in the time-periodic case can be defined in a number of ways. A convenient choice is the curve $p_1q_0p_2$, formed by a segment of the unstable manifold $W^u(p_1)$ and a segment of the stable manifold $W^s(p_2)$. This boundary roughly coincides with the boundary between $\mathcal{R}_1$ and $\mathcal{R}_2$ in the steady case. Inspection of the "A" lobes shows that fluid crosses into $\mathcal{R}_2$ from $\mathcal{R}_1$ only during the mapping from A_0 to A_1 and that fluid leaves $\mathcal{R}_2$ for $\mathcal{R}_1$ only during the B_0-to-B_1 mapping. Thus, fluid enters and leaves $\mathcal{R}_2$ through a "turnstile" mechanism. The associated flux from $\mathcal{R}_1$ to $\mathcal{R}_2$ is calculated by dividing the area of A_0 by the period. In situations where the mapping of fluid lobes is more complicated (such as when A_{-1} maps directly to A_1 and A_0 to A_2) two or more pairs of lobes may cross the boundary during each time period.

Readers unfamiliar with the process and the terminology described above can refer to Guckenheimer and Holmes (1983), Ottino (1989), and Wiggins (1992) for a more general and complete presentation of the material. In the models of Behringer

et al. (1991), Samelson (1992), Meyers (1994), and Duan and Wiggins (1996) this same process is at work, though different approaches and techniques have been utilized to analyze the chaotic motion in each case. Furthermore, these results seem consistent with laboratory experiments showing mixing at the edges of a barotropic jet (Sommeria et al. 1989; Behringer et al. 1991).

The aforementioned kinematic models are limited in that the velocity fields do not obey any dynamical constraints, a shortcoming partially addressed by del-Castillo-Negrete and Morrison (1993) and Pratt et al. (1995) who used linear, dynamical modes to produce meandering velocity fields. In both cases the modes are neutrally stable and have critical lines on either side of the jet axis. Their results also show chaotic exchange but the dynamics are formally valid only for infinitesimal meander amplitude. Furthermore, chaos is diagnosed using the long-time behavior of fluid parcels whereas trajectory calculations in these linear models are formally valid only for finite time. Work along these lines has recently been extended to the weakly nonlinear regime by Ngan and Shepherd (1997) in a critical-level model, but the results still require small amplitudes. There are also a small number of analytical models that employ exact solutions to the fully nonlinear equations of motion, though none involve jets. One is the Kida vortex (Polvani and Wisdom 1990), an elliptical vortex embedded in a constant background shear. The vortex "nutates," a phenomenon of rotation accompanied by periodic variation of the aspect ratio. In a frame of reference rotating with the ellipse, the motion is periodic and the situation is therefore similar to the periodic motion of a jet with an additional meander frequency superimposed on the original steadily propagating meander. Chaotic particle trajectories are found in the region exterior to the Kida vortex.

A significant feature of all periodic models that utilize dynamical modes is that chaos occurs where the potential vorticity gradient is zero. For example, the Kida vortex and the jet examined by Pratt et al. (1995) have piecewise uniform potential vorticity. The jet examined by del-Castillo-Negrete and Morrison (1993) has a background potential vorticity gradient which vanishes along the critical lines where the chaotic motion is centered. These results have been formalized by Brown and Samelson (1994) who show that chaotic motion is precluded (in time-periodic, two-dimensional, incompressible, potential-vorticity conserving flow) in regions of nonzero potential vorticity gradient. As a result, the chaotic motion produces no mixing of potential vorticity nor any potential vorticity fluxes. Indeed, strong potential vorticity gradients have been observed to act as a barrier to mixing in laboratory jets (Sommeria et al. 1989) and the Gulf Stream (Bower and Rossby 1989; Bower and Lozier 1994).

b. Present approach

Our approach overcomes some of the limitations of the simple models described above. In the flow field that is analyzed, the dynamics are fully nonlinear and there is no restriction to small amplitude. The meandering jet flow forms as the result of the growth of initially small amplitude disturbances until saturation occurs. The ultimate meander amplitudes are determined as the result of this evolution, rather than set to arbitrary values (as they are in the linear and kinematic models). Finally, the potential vorticity varies continuously throughout the flow field, in contrast to the artificial piecewise uniform distributions used in several earlier studies.

In the saturated states we consider, the flow field is dominated by a meander of a single wavelength. The spatial structure of the Eulerian flow field remains qualitatively simple; there is no eddy detachment. The meanders propagate eastward at a nearly constant speed and decay slowly due to the presence of weak dissipation. In a frame of reference moving with the average meander speed the time dependence is aperiodic. We have chosen these flow fields for analysis because it is possible to identify in them the prograde (or jet core) region, the recirculations (or cat's eyes), and the retrograde (or far field) regions. The underlying geometry is therefore the same as in the simple models cited above, providing us with the opportunity to verify the fundamental results (that fluid is exchanged between the different regions) in a dynamically consistent setting. At the same time, our flow field presents complications such as aperiodic time dependence and availability of velocity fields over limited time intervals, both of which are more characteristic of oceanic reality. These features necessitate the use and development of new methodology, and this is an important aspect of this work.

Briefly, we use an extended version of a previously described lobe analysis developed for aperiodic flows fields specified over a finite time interval. [Miller et al. (1997) first extended the lobe analysis to the treatment of finite-time data, and Haller and Poje (1998) have strengthened the mathematical underpinnings. The reader is also referred to Nusse and Yorke (1998) and Miller et al. (1997) for background material on the numerical construction of the finite-time geometrical structures. Additional discussion and examples can be found in the recent work by Malhotra and Wiggins (1998).] The results will show that the stretching, stirring, and fluid exchange associated with lobe dynamics is confined to the edges of the recirculations where the potential vorticity gradient is weak, reinforcing the picture that the jet core acts as a barrier to mixing. It will also be shown that these edges are regions of relatively high dissipation of potential vorticity due to filamentation. Estimates of the flux are calculated which, when dimensionalized using scales appropriate to the Gulf Stream, indicate that the transport and exchange due to meandering motions is comparable to the transport associated with warm-core and cold-core ring formation.

Before we continue, we remark that the dynamical systems analysis utilized in this study is just one technique for examining fluid exchange and stirring in flow fields. In addition to providing quantitative estimates of the fluid transport

between different regions of the flow, detailed pictures of the Lagrangian motion result from this analysis. These pictures can be used, for example, to interpret complicated drifter trajectories, as has been done for a set of Gulf Stream RAFOS trajectories (Lozier et al. 1997). However, there are other methods that have their own advantages, and the reader is referred, for example, to the work of Pierrehumbert (1991a, b), Ngan and Shepherd (1997), and references contained therein for analyses that use Lyapunov exponents and Lagrangian statistics to describe mixing.

In the next section we describe the numerical model that has been utilized to generate the flows that are analyzed in this investigation. The finite-time aperiodic analysis that has been applied to the numerical model data is described in section 3, and the results for three meandering jet flows is presented in section 4. In section 5 we discuss the oceanographic relevance of the results and summarize our findings.

2. Numerical framework

Our choice for a model of a meandering jet was dictated by the need to capture some of the properties of Gulf Stream meanders (eastward phase propagation, finite amplitude), to achieve dynamical consistency, and, at the same time, to maintain a link with existing simple models (limited number of wavelengths present and well-defined retrograde, prograde, and recirculating regions). Flow fields that fit these requirements were found by Flierl et al. (1987) in their study of barotropic, β-plane jets. They numerically simulated the evolution of an unstable jet disturbed by a small amplitude perturbation in order to identify regimes in which eddy detachment would occur. In addition to spin-off eddies, they found a variety of other regimes including finite-amplitude meandering states, vortex streets, dipoles, and various instabilities (see Fig. 3 ⊙►). Using higher resolution, longer computation times, and a different type of dissipation, we have recomputed three of their finite-amplitude meandering states and we will base our lobe analysis on these simulations.

The flow fields we analyze are numerically approximated solutions of the barotropic, β-plane, potential vorticity equation,

$$\frac{\partial q}{\partial t} + J(\psi, q) = \mathcal{D} \qquad (1)$$

with periodic boundary conditions in both zonal and meridional directions. In (1), ψ is the streamfunction, $q = \nabla^2\psi + \beta y$ is the potential vorticity, β is the variation of the Coriolis parameter with latitude, $J(\psi, q) = (\partial\psi/\partial x)(\partial q/\partial y) - (\partial\psi/\partial y)(\partial q/\partial x)$ is the Jacobian of ψ and q, and $\mathcal{D}$ is a dissipation term. Equation (1) is viewed as nondimensional, with length, velocity, and time scales L^*, U^*, and L^*/U^*, respectively, where L^* is representative of the half-width of the jet and U^* is the maximum jet velocity. The flow is approximated pseudospectrally in a square computational domain of nondimensional length L_D and is allowed to develop from a weakly perturbed zonal jet of the form,

$$\psi(x, y, t = 0) = -\mathrm{erf}(y) + 2y/L_D + \varepsilon e^{-y^2}\sin(k_0 x)(2)$$

with $\varepsilon = 0.02$ and wavenumber $k_0 = 2\pi n_0/L_D$. Flierl et al. (1987) found that $(\beta, k_0) = (0.103, 0.74)$ and $(\beta, k_0) = (0.207, 0.98)$ lead to finite-amplitude meandering states in which the flow is dominated by a meander with wavelength equal to the initial perturbation. An example of the development of this meandering state is shown in Fig. 4 ⊙►.

Using a dimensional value of $\hat{\beta} = 1.8 \times 10^{-11}$ m^{-1} s^{-1} $= \beta U^*/L^{*2}$, we associate $\beta = 0.103$ with the scales $U^* = 175$ cm s^{-1}, $L^* = 100$ km, and $t^* = L^*/U^* = \frac{2}{3}$ day, and $\beta = 0.207$ with the scales $U^* = 87$ cm s^{-1}, $L^* = 100$ km, and $t^* = L^*/U^* = 1\frac{1}{3}$ day. These scales are associated with propagation speeds that are higher than the speeds observed for Gulf Stream meanders by Lee and Cornillon (1996) using satellite imagery. Between 75° and 45°W, they find speeds less than 6 km d^{-1} for the 650–800 km wavelengths corresponding to the meanders in our numerical solutions, which propagate at 12 to 18 km d^{-1}. This discrepancy is probably due to the fact that Gulf Stream meanders have a significant baroclinic component. We also note that Gulf Stream meanders are unrestricted by periodic boundary conditions. It is unlikely that the clean, nearly monocromatic meanders of the type considered in this study would exist for long in such a setting, and we therefore view the model flow as a stepping stone to more complicated situations.

A common problem in spectral approximations is the amplification of high modes associated with Laplacian-type operators, resulting in numerical instability. One method used to control this amplification is to model diffusion in terms of a superviscosity ($\mathcal{D} = -v_4\nabla^6\psi$), as was done in Flierl et al. (1987). An alternative approach employs a filter to selectively damp only the high modes. In this study, we have applied a weak exponential cutoff filter to the Fourier projection of the potential vorticity field to control numerical instability. The form of this filter in terms of the normalized wavenumber $\theta_i = L_D k_i^H/N = 2\pi i/N$, $i = 0, \ldots, N/2$, is (see Canuto et al. 1988)

$$\sigma(\theta_i) = \begin{cases} 1 & \text{for } |\theta_i| < \theta_c \\ e^{-\alpha(|\theta|-\theta_c)^8} & \text{for } \theta_c \leq |\theta_i| \leq \pi, \end{cases} \qquad (3)$$

where $k^H{}_i = 2\pi i/L_D$ is the discretized wavenumber in the x or y direction, and we have set $\theta_c = 0.65\pi$ and $\alpha = 37 \approx -\ln$ (10^{-16}). Since the use of the filter introduces some (albeit small) numerical dissipation, we have chosen to model the physical dissipation of potential vorticity,

$$\mathcal{D} = \frac{1}{\text{Re}}\nabla^4\psi, \qquad (4)$$

where $\text{Re} = U^*L^*/A$ is the Reynolds number. The flows are computed at two Reynolds numbers, $\text{Re} = 10^3$ and $\text{Re} = 10^4$, corresponding to eddy viscosities $A = 175 \text{ m}^2 \text{ s}^{-1}$ ($17.5 \text{ m}^2 \text{ s}^{-1}$) and $A = 87 \text{ m}^2 \text{ s}^{-1}$ ($8.7 \text{ m}^2 \text{ s}^{-1}$) for $\beta = 0.103$ and $\beta = 0.207$, respectively, at $\text{Re} = 10^3$ ($\text{Re} = 10^4$). The solutions presented were computed pseudospectrally using $N = 128$ Fourier modes in the zonal and meridional directions on a square computational domain with nondimensional length $L_D = 25.6$, and advanced in time using leapfrog time stepping with occasional Euler correction and time step $\Delta t = 0.025$. The resolution is such that, for the Reynolds numbers used, the physical dissipation dominates the numerical dissipation associated with the filter, resulting overall in approximately 1% (10%) total kinetic energy loss per 100 nondimensional time units for simulations with $\text{Re} = 10^4$ ($\text{Re} = 10^3$).

Three flows are analyzed in this study, corresponding to the following parameter settings,

Case I: $(\text{Re}, \beta, k_0) = (10^4, 0.103, 0.74)$

Case II: $(\text{Re}, \beta, k_0) = (10^4, 0.207, 0.98)$

Case III: $(\text{Re}, \beta, k_0) = (10^3, 0.103, 0.74)$.

As an example, the evolution of the flow for parameter setting III is shown in Fig. 4 ⊙ in terms of the potential vorticity field. The initial weakly perturbed zonal jet [Eq. (2)] is unstable and develops nonlinearly into a finite-amplitude meandering configuration. The generation and evolution of coherent structures in the flow for times $t = 0$ to $t \approx 100$ is discussed in detail by Flierl et al. (1987). By time $t_0 = 200$ in this case (Fig. 4b ⊙), the flow has saturated into a configuration characterized by large-scale meanders that propagate eastward at a nearly constant speed and decay in amplitude as time progresses. It is in this regime that the numerical flows are analyzed. In some cases, secondary instabilities occur causing pairing of the meanders and generation of longer wavelengths. This stage of evolution, which begins for simulation times on the order of 500–1000, is avoided in our analysis.

Table 1 ⊙ lists the simulation times t_0 that have been chosen as the initial times for the analysis in each case. These times have been subjectively chosen and no rigorous selection criterion has been applied. To examine the Lagrangian motion in the three flows, it is convenient to view the flows in a reference frame moving with the large-scale meanders. The propagation speed of the large-scale meanders has been estimated by spatially averaging over a portion of the domain ($-4.4 < y < 4.4$) the difference of the streamfunction, velocity, and vorticity fields at times $t > t_0$ with fields at time t_0 until a best fit (a minimization of the spatially averaged difference) was located. The reference-frame translation speeds that have been selected for each of the three flows analyzed are listed in Table 1 ⊙. Spectral analysis could also be utilized since the large-scale meanders are dominated by a single meandering mode. For parameter setting III, for example, time series of the meridional velocity at two fixed locations, $(x, y) = (6.0, 12.8)$ and $(x, y) = (8.0, 15.0)$, reflect the propagation of the jet meanders past these locations (see Fig. 5a ⊙). The power spectra of both time series (Fig. 5b ⊙) show distinguished peaks near $\omega/(2\pi) = 0.0138$, indicating a propagation speed of $c = (L_D/n_0)\omega/(2\pi) = 0.1178$. We remark that a precise determination of the propagation speed is not essential to the characterization of the lobe dynamics presented in the following sections. Viewing the flow in a reference frame translating with the large-scale meanders simply makes it easier to identify the regions in the flow that exhibit the strong hyperbolicity necessary for the construction of the stable and unstable surfaces.

Figure 4b ⊙ also shows patches of vorticity swirling around within the recirculation regions, a motion that is evidence of a second important time dependency. (One patch is marked in the figure with asterisks.) The vortical regions undergo a nutation (a rotation accompanied by a change in aspect ratio similar to that of the Kida vortex) concurrent with an amplitude

pulsation of the large-scale meanders. The time dependence of this motion can be quantified by computing the spatially averaged norm described above, or by conducting a similar spectral analysis, for the flow in the moving reference frame. For example, the spectral analysis for parameter setting III is shown in Fig. 6 ⊙. The highest peaks in the spectra coincide with the period of nutation, a feature found in all three flows studied. (The secondary peaks in Fig. 6b ⊙ are harmonics.) The time periods associated with the nutation are listed in Table 1 ⊙ for each of the three flows analyzed. We document this phenomena to give the reader a feeling for the time dependence in the moving frame. However, the analysis presented below does not require the presence of any characteristic time scale.

In the next section, we describe the analysis that has been conducted on the numerical model data. In each case, the flows are analyzed over a finite time interval spanning 250 nondimensional time units (that is, over the time interval $t = [t_0, t_0 + 250]$). Although t_0 is different for each of the parameter settings analyzed, for convenience throughout the rest of the paper we will refer to the time interval over which the analysis is conducted as $t = [0, T_f]$ for each case.
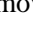
3. Aperiodic analysis

It is possible to carry out the same type of lobe analysis for the aperiodic flow that was described in section 1 for periodic flow, provided generalizations of hyperbolic points and their stable and unstable manifolds can be found. Recall that a hyperbolic point corresponds to a particular fluid trajectory that passes the same location periodically. Such points are found just to the north of meander crests (and the south of troughs) of the jet. Nearby trajectories converge and diverge toward or away from this trajectory along its stable and unstable manifolds, respectively. In the aperiodic case it is reasonable to expect similar structures to arise, given the geometrical similarity with the periodic case. Specifically, one might expect to find a distinguished trajectory, $\gamma(t)$, in the region north of a meander crest that remains in the general area and is characterized by converging and diverging Lagrangian motion in its immediate neighborhood. We call $\gamma(t)$ a hyperbolic trajectory. Stable and unstable manifolds W^s and W^u are then defined as the collection of trajectories that converge to $\gamma(t)$ as $t \rightarrow \infty$ and as $t \rightarrow -\infty$, respectively. Unlike the periodic case, these surfaces must be visualized in the full three-dimensional space (x, y, t). Figure 7 ⊙ shows a hypothetical example with the hyperbolic trajectory labeled $\gamma(t)$ and its stable and unstable manifolds indicated by blue and red surfaces, respectively. Intersection between the stable and unstable manifolds of different hyperbolic trajectories can be used to identify material lobes of fluid trapped between the two surfaces and whose motion can be followed in the same manner as before. The intersecting surfaces might look something like the ones drawn in Fig. 8a ⊙. Whether this exercise is helpful in clarifying transport and stirring processes in the flow field depends on the complexity of the flow field under consideration.

Unfortunately, velocity fields defined over $-\infty < t < \infty$ are typically available only in highly idealized models. In most imaginable examples based on numerical or real data, the velocity fields will be available over only a finite time, and it will not be possible to formally identify stable and unstable manifolds in terms of infinite time limits. However, it is possible to identify material surfaces that approximate the stable and unstable manifolds, which presumably could be found provided the full ($-\infty < t < \infty$) time record was available. The construction of these material surfaces is described below. [The reader is also referred to Nusse and Yorke (1998), Miller et al. (1997), and Haller and Poje (1998) for more detailed and rigorous discussions.]

Suppose that data over a finite time interval, $0 \leqslant t \leqslant T_f$, is given and regions of strong hyperbolicity are identified, such as to the north of the meander crests. Then, as depicted schematically in Fig. 7a ⊙, a surface $W^s(x, y, t)$ can be generated by evolving in backward time a short segment of particles initially located in the region and aligned in the stable direction. The initial placement of the line of particles is such that the end points stretch in opposite directions and the surface W^s continues to straddle the particular hyperbolic region for all $0 \leqslant t \leqslant T_f$. A second surface $W^u(x, y, t)$ is generated by evolving forward in time a segment of particles initially located in a region of strong hyperbolicity at time $t = 0$ and aligned in the unstable direction (see Fig. 7b ⊙). Initializing the surface W^u so that it includes the *same* hyperbolic region used to generate W^s ensures that there will be intersections between W^u and W^s. Moreover, there will be *exactly one* intersection that remains in a "small" neighborhood of the hyperbolic region for the entire time interval. We will refer to such an intersection as a *distinguished hyperbolic trajectory,* denoted as $\gamma(t)$ (see Fig. 7b ⊙). The corresponding stable and unstable surfaces are denoted as W^s_γ and W^u_γ, respectively. By construction, all trajectories on the material surface W^s_γ approach $\gamma(t)$ as time progresses ($t \rightarrow T_f$) and all trajectories on W^u_γ approach $\gamma(t)$ as time regresses ($t \rightarrow 0$). Therefore, these surfaces serve as approximate stable and unstable manifolds for the distinguished hyperbolic trajectory $\gamma(t)$.

In this manner, every distinct hyperbolic region in the meandering jet flow can be identified with a distinguished hyperbolic trajectory, denoted γ_i, and with approximate stable and unstable manifolds denoted $W^s_{\gamma_i}$ and $W^u_{\gamma_i}$, for which

$\gamma_i = W^s_{\gamma_i} \cap W^u_{\gamma_i}$. For the meandering jet flow, stable and unstable manifolds have been computed for two hyperbolic trajectories, $\gamma_1(t)$ and $\gamma_2(t)$, north of consecutive meander crests. The fluid exchange between the northern recirculation region and the adjacent retrograde region is described in terms of the surfaces $W^s_{\gamma_1}$ and $W^u_{\gamma_2}$, shown schematically in Fig. 8a ⊙. Fluid particles that move toward γ_1 as time progresses lie on the surface $W^s_{\gamma_1}$, shown in blue. Particles that move away from γ_2 as time progresses lie on the surface $W^u_{\gamma_2}$, shown in red. The surfaces intersect traversely in the x–y plane. At a given time in the x–y plane, the intersections terminate segments of the stable and unstable curves that bound areas of fluid called "lobes" (two lobes, marked **A** and **B**, are labeled in Figs. 8a,b ⊙). Since the surfaces are composed of Lagrangian trajectories, the fluid within the lobes can be tracked throughout the time interval once the surfaces are known. As the lobes evolve in time, their shape can deform considerably but, due to the incompressibility of the flow, the area of an individual lobe remains constant. In regions of strong hyperbolicity, found in the vicinity of γ_1 and γ_2 for example, the boundaries of lobes undergo rapid stretching, and we can expect their shapes to become severely filamented as in the case of periodic time dependence.

In order to discuss fluid exchange between the different regions of the flow, the boundaries between the regions must be defined. Referring to Figs. 8a,b ⊙ let $W^s_{\gamma_1,t_0}$ denote the curve that is the $t = t_0$ time slice of the surface $W^s_{\gamma_1}$, and similarly for $W^u_{\gamma_2,t_0}$, that is,
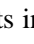
$$W^s_{\gamma_1,t_0} \equiv W^s_{\gamma_1}(x,\, y,\, t = t_0)$$

$$W^u_{\gamma_2,t_0} \equiv W^u_{\gamma_2}(x,\, y,\, t = t_0).$$

Furthermore, let $W^s_{\gamma_1,t_0}[p,\, q]$ denote the segment of $W^s_{\gamma_1,t_0}$ between the points p and q, and similarly for $W^u_{\gamma_2,t_0}[p,\, q]$. The regime boundary between the recirculation region and the retrograde region at time $t_0 \in [0,\, T_f]$ is then defined as

$$\mathcal{B}(t = t_0): \quad W^s_{\gamma_1,t_0}[\gamma_1,\, q] \cup W^u_{\gamma_2,t_0}[q,\, \gamma_2], \quad (5)$$

where q is an intersection point of $W^s_{\gamma_1,t_0}$ and $W^u_{\gamma_2,t_0}$. We select the intersection point that produces a boundary resembling the cat's eye structure in the steady flow. In Fig. 8a ⊙ for example, the boundary at time $t = 0$ is defined in terms of the intersection point labeled "q_0." As time progresses however, the boundary deforms and in order to restore symmetry to the shape of the boundary, another intersection point, q_{-1}, is eventually chosen to define the new boundary. That is,

$$\mathcal{B}(t): \begin{cases} W^s_{\gamma_1,t}[\gamma_1,\, q_0] \cup W^u_{\gamma_2,t}[q_0,\, \gamma_2] & \text{for } t \in [0,\, t_1) \\ W^s_{\gamma_1,t}[\gamma_1,\, q_{-1}] \cup W^u_{\gamma_2,t}[q_{-1},\, \gamma_2] & \text{for } t \in [t_1,\, t_2) \\ \quad \vdots & \quad \vdots \end{cases}$$

Therefore, the regime boundary is defined discontinuously in time. (Notice that in Figs. 8a,b ⊙ and in the definition above the index of q_i is incremented for every *second* intersection point.) The redefinition of the boundary results in a fluid exchange "across" the boundary involving a pair of lobes called "turnstile lobes." (Transport occurs only where the boundary is redefined, which is generally away from the hyperbolic trajectories.) Referring to Fig. 8b ⊙, the fluid in lobe A, which is north of the boundary (and therefore in the retrograde region) for times $t \in [t_0,\, t_1)$, is "transported" south of the boundary (and therefore into the recirculation region) at time $t = t_1$ when the intersection point with which the boundary is defined is switched. Meanwhile, the fluid in lobe B is transported from the recirculation region to the retrograde region. Since the fluid in lobe A is trapped south of $W^u_{\gamma 2}$ and north of $W^s_{\gamma 1}$ for the entire available time interval ($t \in [0,\, T_f]$), there would be no fluid exchange if the chosen intersection point with which the boundary is defined remained unchanged.

In the traditional time-periodic or quasiperiodic analysis, the boundary across which the exchange occurs is also defined discontinuously in time. In a time-periodic flow, the structure of the material surfaces are replicated at constant time

intervals equal to the time period of the flow. The intersection point with which the boundary is defined is switched at these regular time intervals, yielding a boundary that is exactly the same as the boundary at the beginning of the interval. In the aperiodic flow, the timing of the boundary redefinition is less obvious. Since the meandering jet flow in this study is spatially symmetric in the large-scale sense, the redefinition of the boundary has been selected to approximately coincide with the time when an intersection point is midway between the meander crests. The resulting boundary at time t_{i+1} has the same cat's eye shape as the boundary at time t_i, but the two boundaries are not identical. Alternatively, the timing of the boundary redefinition could be chosen to coincide with a characteristic time period such as the nutation period. Note that the discontinuous alteration of the boundary occurs well away from the hyperbolic trajectories so that the motion of the latter do not effect the transport.

4. Transport in the aperiodic flow

The aperiodic analysis described in the previous section has been applied to three meandering-jet flows corresponding to the parameter settings,

$$\text{Case I:} \quad (Re, \beta, k_0) = (10^4, 0.103, 0.74)$$

$$\text{Case II:} \quad (Re, \beta, k_0) = (10^4, 0.207, 0.98)$$

$$\text{Case III:} \quad (Re, \beta, k_0) = (10^3, 0.103, 0.74).$$

In this section, we present results illustrating the fluid exchange across the regime boundary separating the recirculation region and the retrograde region, as represented by intersections of the surfaces $W^s_{\gamma_1}$ and $W^u_{\gamma_2}$, for one recirculation region on the northern side of the jet. The exchange between the jet core and the recirculation region, represented by the intersecting surfaces $W^u_{\gamma_1}$ and $W^s_{\gamma_2}$, is significantly less than that across the recirculation–retrograde boundary for each of the three cases; results showing jet core–recirculation exchange will be presented at the end of this section for parameter setting III only.
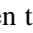
a. Case I: (Re, β, k₀) = (10⁴, 0.103, 0.74)

The results of the analysis for this case are shown in Fig. 9 ⊙. At selected times, time slices through the intersecting surfaces $W^s_{\gamma_1}$ and $W^u_{\gamma_2}$ are shown and the areas, or lobes, delineated by the intersecting curves are color filled.
Included in the plots are contours, drawn in the dotted line style, of the potential vorticity field in the moving reference frame north of the jet axis. The locations of two distinguished hyperbolic trajectories are marked in the figures with the "+" symbol, and in the discussion that follows we refer to the one north of the westernmost meander crest depicted in the figures as γ_1 and to the one north of the easternmost meander crest as γ_2. The point marked with an asterisk distinguishes the intersection point q, chosen to define the regime boundary at the displayed time. The boundary is drawn in the figures with a thick black line. To ease the discussion that follows and help the reader decipher the figures, each lobe is numbered individually and tagged with one of six colors.

As noted in the previous section, the curves $W^s_{\gamma_1,t}$ and $W^u_{\gamma_2,t}$ become severely filamented near the hyperbolic regions γ_2 and γ_1, respectively. This filamentation can be so extreme that the accuracy of the computation is insufficient to be reliable and the structures lose their physical relevance. Therefore, we have deleted portions of $W^s_{\gamma_1,t\approx 0}$ and $W^u_{\gamma_2,t\approx T_f}$ in the vicinity of γ_2 and γ_1, respectively. Even though an infinite number of lobes theoretically exist throughout the entire available time interval, the result of truncating $W^s_{\gamma_1}$ and $W^u_{\gamma_2}$ is that only a finite number of lobes can be identified and the identified lobes are visible in the figures for only a portion of the available time interval, appearing near γ_2 at early times and then disappearing near γ_1 at late times after moving cyclonically along the northern recirculation–retrograde boundary. In addition, a consequence of the method used to compute the material surfaces (see section 3 and Fig. 7 ⊙) is that only a small segment of the curve $W^u_{\gamma_2,t}$ is known at times near the beginning of the available time interval and only a small segment of $W^s_{\gamma_1,t}$ is known at times near the end of the interval. In the first frame in Fig. 9 ⊙ corresponding to time $t = 38$, the curve

$W^s_{\gamma_1, t=38}$ has been truncated near γ_2 and only the segment of the curve $W^u_{\gamma_2, t=38}$ between q and γ_2 is known. Therefore only six lobes are identified at time $t = 38$. At later times additional lobes are identified, and as the lobes move towards γ_1 they eventually disappear from the figures as $W^u_{\gamma_2, t}$ is truncated. Near the end of the available time interval, no newly identified lobes are present in the figures since only a short segment of $W^s_{\gamma_1, t \approx T_f}$ is known (see last two frames in Fig. 9 ◔).

According to the chosen regime boundary at time $t = 38$ (first frame in Fig. 9 ◔), lobes 1 (purple), 3 (blue), and 5 (too thin to recognize the coloring) are in the retrograde region while lobes 2 (red), 4 (pink), and 6 (yellow) are in the recirculation region. As time progresses, the fluid within the lobes moves cyclonically (counterclockwise). After advecting westward, lobe 1 at time $t = 72$ is stretched eastward around the southern edge of the recirculation region, becoming thin and elongated. In contrast, lobes 2, 3, and 4, which were filamented at time $t = 38$, have formed into more compact shapes by $t = 72$. Furthermore, two of the lobes have moved into a different flow regime; the fluid within lobe 1 has moved from the retrograde region of the flow into the recirculation region, while the fluid in lobe 2 has moved from the recirculation region to the retrograde region. (Note that, as discussed in the previous section, a new intersection point has been chosen to define the boundary at time $t = 72$.) Therefore, over the time interval $t \in [38, 72]$ there has been an *exchange* of fluid between the recirculation and retrograde regions. The exchange process between the recirculation and retrograde regions continues as time progresses. Between times $t = 72$ and $t = 98$ in Fig. 9 ◔, lobe 3 (blue) moves from the retrograde region to the recirculation region while lobe 4 (pink) moves from the recirculation region to the retrograde region. Meanwhile, lobes 1 and 2 remain in the recirculation and retrograde regions, respectively, and are compressed and stretched as their associated intersection points move towards γ_1.

The snapshots in Fig. 9 ◔ correspond to the times that we have chosen to redefine the regime boundary (that is, when every second intersection point crosses midway between meander crests). The time period that was found to dominate the flow in the moving reference frame, $T = 52.5$ (see Table 1 ◔), is almost twice as long as the time interval between snapshots in Fig. 9 ◔. After some study, it can been seen that the overall lobe structure is qualitatively replicated at every *second* snapshot shown. That is, the lobe pattern in the snapshots at $t = 38$, $t = 98$, $t = 156$, and $t = 210$ resemble each other (disregarding the absence of unidentifiable lobes at $t = 38$ and $t = 210$); there is an approximately repeatable pattern every cycle, where the cycle length varies from 60 early in the available time interval to 54 at the end of the available time interval. In this flow, *two sets* of lobes (i.e., four lobes) participate in the exchange process during each cycle. In the first cycle ($t \in [38, 98]$), lobes 1, 2, 3, and 4 participate in the exchange. During the second cycle ($t \in [98, 156]$), the exchange is represented by the movement of lobes 5 (green) and 6 (yellow) (see frames $t = 98$ and $t = 130$) and by lobes lobes 7 (purple) and 8 (red) (see frames $t = 130$ and $t = 156$), and so on. If the flow were precisely time-periodic with a (constant) period of 60 for example, then the lobe structure would be *exactly* replicated every 60 time units. The region occupied by lobes 1, 2, 3 and 4 at time $t = 38$ would be occupied by lobes 5, 6, 7, and 8, respectively, at time $t = 98$, followed by lobes 9, 10, 11, and 12 at time $t = 158$, and so on. That is, if the flow were time-periodic there would be a mapping of the lobes in four groups,

$$\text{group A:} \quad 1 \rightarrow 5 \rightarrow 9$$
$$\text{group B:} \quad 2 \rightarrow 6 \rightarrow 10$$
$$\text{group C:} \quad 3 \rightarrow 7 \rightarrow 11$$
$$\text{group D:} \quad 4 \rightarrow 8 \rightarrow 12,$$

such that within a given group the lobes have exactly the same size and shape. Table 2 ◔ lists the lobe areas that have been calculated for each of the lobes depicted in Fig. 9 ◔.[1] Since the flow in this case is not time-periodic, the lobe structure is not precisely replicated and the lobe areas within each group are not constant. Over the first cycle ($t = 38$–98; lobe 1 → 5, 2 → 6, 3 → 7, 4 → 8) there is a 9% contraction of the overall lobe structure, while over the second cycle ($t = 98$–156; lobe 5 → 9, 6 → 10, 7 → 11, 8 → 12) there is a 34% increase of the total lobe area.

The size of the lobes also indicates how much fluid is participating in the exchange between different regions of the flow. Over each cycle, the transport between the two regions can be computed by simply dividing the area of the lobes participating in the exchange by the length of the cycle. As described above, two sets of lobes participate in the exchange between the recirculation and retrograde regions over each cycle for the case shown in Fig. 9 ◔. The cumulative area from both sets of lobes and the transport to/from the recirculation from/to the retrograde region during the cycle are listed in Table 3 ◔. Over each cycle, there is a net transport from the recirculation region to the retrograde region. Note that this is *not* a net mass transport across a fixed boundary, but rather a net change in the type of motion exhibited by fluid particles in the vicinity of the cat's eyes. That is, as time progresses, more fluid undergoes a change from recirculating motion to

retrograde motion than vice versa.

b. Case II: (Re, β, k_0) = (10^4, 0.207, 0.98)

The results of the aperiodic analysis for the flow corresponding to the second case are shown in Fig. 10 . In the first time frame displayed, $t = 38$, seven lobes have been identified although lobe 5 is too small to be distinguished in the figure. Over the time interval $t \in$ [38, 64], the fluid in lobe 2 (red) moves from the retrograde region to the recirculation region, while the fluid in lobe 3 (blue) moves from the recirculation region to the retrograde region. Over the next time interval $t \in$ [64, 96], however, *two* sets of lobes participate in the exchange: lobes 4 (pink) and 5 (hidden at $t = 64$), and lobes 6 (yellow) and 7 (purple). At regular intervals thereafter ($\delta t = t_2 - t_1 = 32$), the exchange between the recirculation and retrograde regions is again accomplished by just *one* set of lobes. Over the time interval $t \in$ [96, 128], the exchange is represented by the movement of lobes 8 (red) and 9 (blue), and for $t \in$ [128, 164] lobes 10 (pink) and 11 (green) perform the exchange, and so on.

That two sets of lobes pass through the turnstile during the time interval $t \in$ [64, 96] is a consequence of the temporal aperiodicity of the flow. Also, unlike the previous case for which the qualitative pattern of the lobe structure was approximately repeated, the time dependence in this case obscures any such pattern in the lobe structure. Although the lobes in the groupings,

$$\text{group A:} \quad 8 \to 10 \to 12$$
$$\text{group B:} \quad 9 \to 11 \to 13,$$

have comparable areas (see Table 4), the shapes of the lobes do not correspond as well (see $t = 128$, $t = 164$ and $t = 196$ snapshots in Fig. 10).

The recirculation–retrograde transport during each cycle is summarized in Table 5 . The direction of the net transport varies for the different cycles, but the net cumulative transport over the time interval $t \in$ [38, 228] is from the recirculation region to the retrograde region. Notice that, even though two sets of lobes participate in the exchange over the interval $t \in$ [64, 96], lobes 4 and 5 are small and do not inflate the transport over this time interval.

c. Case III: (Re, β, k_0) = (10^3, 0.103, 0.74)

The results for the third case are shown in Fig. 11 . In this case, the Reynolds number has been decreased by a factor of 10 from case I and, in a broad sense, the evolution of the lobe structure shown in Fig. 11 is similar to that shown in Fig. 9 . Over the time interval between successive snapshots in Fig. 11 , one set of lobes is transported across the recirculation–retrograde boundary; lobes 1 (purple) and 2 (red) are transported across the regime boundary during $t \in$ [48, 80], followed by lobes 3 (blue) and 4 (pink) during $t \in$ [80, 102], and lobes 5 (green) and 6 (yellow) during $t \in$ [102, 134], and so on.

Like case I, there is a repeatable pattern to the qualitative lobe structure (the snapshots at $t = 48$, $t = 102$, and $t = 162$ resemble each other, as do those at $t = 80$, $t = 134$, and $t = 194$) but the size of the lobes resident along the northern edge of the cat's eye decrease considerably as time progresses. We can again consider the mapping of lobes into four groups,

$$\text{group A:} \quad 1 \to 5 \to 9$$
$$\text{group B:} \quad 2 \to 6 \to 10$$
$$\text{group C:} \quad 3 \to 7 \to 11$$
$$\text{group D:} \quad 4 \to 8.$$

Referring to Table 6 , which lists the computed lobe areas for this case, there is a 27% contraction of the overall lobe structure over the first cycle ($t = 48–102$; lobe $1 \to 5$, $2 \to 6$, $3 \to 7$, $4 \to 8$) and a 33% contraction over the second cycle [$t = 102–162$; lobe $5 \to 9$, $6 \to 10$, $7 \to 11$, $8 \to 12$ (assuming lobe 12, which is not identified, has the same area as lobe 8)].

The transports to/from the recirculation from/to the retrograde region over the time intervals displayed in Fig. 11 are summarized in Table 7 . Since the lobes that participate in the exchange decrease in size as time progresses, the transport across the regime boundary decreases with time. As in the low-dissipation case, more fluid undergoes a change from

recirculating motion to retrograde motion during each cycle than vice versa.

The results presented above detail the evolution of the intersecting surfaces $\mathcal{W}^s_{\gamma_1}$ and $\mathcal{W}^u_{\gamma_2}$, providing a description of the fluid exchange between the recirculation and retrograde regions. The exchange between the jet core and the recirculation region can be similarly analyzed by computing the intersecting surfaces $\mathcal{W}^u_{\gamma_1}$ and $\mathcal{W}^s_{\gamma_2}$. Figure 12 shows the results of the jet core–recirculation analysis for case III. Eight individual lobes are formed in the available time interval, but most of the time the lobes are so thin that the intersection points and the identifying color cannot be detected in the figure. The computed lobe areas are listed in Table 8. Compared to the lobes formed along the northern edge of the cat's eye (see Fig. 11 and Table 6), these lobes are a factor of 7 smaller (using the average area of lobes 1, 2, 3, and 4 as representatives). Likewise, the associated transport between the jet core and the recirculation region, listed in Table 9, is several times smaller than the transport between the recirculation and retrograde regions. Analyses of the jet core–recirculation exchange for cases I and II yield similar results (not shown).

5. Discussion and summary

The structures that have been computed in the analysis presented above are constructs that enable certain key Lagrangian features of the meandering jet flow to be described in detail. The geometry of these structures illustrates how patches of fluid are stretched, stirred, and transported to different regions in the flow. In Figs. 9–12 it can also be seen that the stable and unstable surfaces are embedded within regions of relatively low potential vorticity gradient. In particular, the dynamics do not allow the material surfaces to penetrate the high potential-vorticity-gradient region of the jet, reinforcing the picture that the jet core acts as a barrier to mixing.

Since the lobes undergo filamentation, it is natural to ask whether the regions occupied by the lobes are ones of high dissipation. The process of filamentation acts to increase local property gradients (e.g., potential vorticity gradients) and can thereby facilitate changes in the property field by locally increasing the dissipation. To address this question, additional numerical computations were conducted to study the potential vorticity evolution of Lagrangian particles in this nonconservative system. In these experiments, the flows for cases I and III were seeded with fluid particles along two meridional lines that transect the cat's eye region (see Fig. 13). The fluid particles were initialized at time $t = 98$ for case I and at time $t = 102$ for case III, and numerically tracked for 200 nondimensional time units. The potential vorticity of each fluid particle was computed as the numerical flow field was advanced in time by interpolating the potential vorticity field to the particle location using the same sixth-order Lagrange algorithm used to estimate the Lagrangian velocity. The resulting potential vorticity time series for each particle was then analyzed in a simple fashion in an attempt to quantify the nonconservation of potential vorticity for the Lagrangian fluid particles. Figures 14 and 15 show the mean potential vorticity and standard deviation computed for each particle trajectory for cases I and III, respectively.

Overall, fluid-particle potential vorticity variations are weak, with standard deviations for case III (with Re = 10^3) somewhat higher than for case I (with Re = 10^4) as might be expected due to the increased physical dissipation in the flow (Figs. 14b,c and Figs. 15b,c). However, for both Reynolds numbers the potential vorticity variations appear to have some spatial dependence. An inspection of the potential vorticity time series for the particles reveals that while many of the time series exhibit a general downward trend, some of the fluid particles exhibit relatively large rapid transitions in their potential vorticity. For case I (with Re = 10^4), we have subjectively singled out particles that exhibit potential vorticity changes of $\Delta q > 0.01$ over any 10-unit time interval, and have applied the criterion $\Delta q > 0.015$ over a 10-unit time interval for case III (with Re = 10^3). These particles are highlighted in Figs. 14b,c and Figs. 15b,c with a square plot marker. While this selection process does include the particles with the largest rms potential vorticity fluctuations, which would manifest if the potential vorticity jumps were very large, it also includes particles that have relatively moderate standard deviations, differentiating them from trajectories that exhibit trends in potential vorticity. The initial locations of these same selected particles are marked in Fig. 13 with an asterisk. Also shown in Fig. 13 are snapshots of the lobe structure for cases I and III at the time the particles were initialized. There is a striking correspondence between the initial locations of particles that undergo rapid potential vorticity changes and regions demarcated by the lobe structure. [Recall that only a subset of the lobes that exist are actually depicted in the snapshots, so it is possible that the particle locations near $(x, y) = (14, 16)$ in Fig. 13a and near $(x, y) = (17.5, 14)$ in Fig. 13b also coincide with a portion of the entire lobe structure.] The correlation suggests that the filamentation experienced by the evolving lobes is associated with increased dissipation and eventual mixing.

In addition to revealing how the Lagrangian motion is geometrically constrained, the analysis we have conducted provides quantitative estimates of the fluid exchange between regions of the flow exhibiting qualitatively different types of motion. In all of the cases studied here, the most significant fluid exchange takes place between the recirculation regions located on both sides of the meandering jet and the retrograde region in the far field. Exchange between the recirculation regions and the jet occurs in a narrow region along the edge of the jet core, away from the strong potential vorticity gradients associated with the core of the jet, and is associated with a transport estimate that is approximately 4 or 7 times smaller than the

transport between the recirculation and retrograde regions.

The amount of fluid participating in these exchange processes can be dimensionalized to provide transport estimates appropriate for the Gulf Stream. The dimensional volume transport is

$$\hat{\mathcal{T}} = L^* U^* D^* \mathcal{T},$$

where $\mathcal{T}$ is the nondimensional transport, L^* is the length scale representative of the half-width of the jet, U^* represents the maximum jet velocity, and D^* represents the depth over which the transport takes place. Using $L^* = 100$ km and $U^* = 175$ cm s^{-1} ($U^* = 87$ cm s^{-1}) for nondimensional $\beta = 0.103$ ($\beta = 0.207$) (see section 2) and taking $D^* = 500$ m as a representative value for the thickness (Lai and Richardson 1977), the results listed in Tables 3, 5, and 7 yield dimensional transports on the order of 0.5 to 4 Sv (Sv $\equiv 10^6$ m^3 s^{-1}) over one meander wavelength. The transport associated with Gulf Stream ring detachment could be estimated at approximately 1 to 5 Sv, assuming an average formation rate of five to six rings per year over distances comparable to the meander wavelength of the numerical jet, an average ring diameter of 130–250 km and a thickness of 500 m (Lai and Richardson 1977; Auer 1987). Of course, the formation of Gulf Stream rings results in a fluid exchange that is entirely different from the transport discussed here, and the above comparison is simply meant to put the current results in perspective. Rings generally carry large volumes of fluid from one side of the Gulf Stream to the other, whereas the Lagrangian transport described herein is associated with stirring and transport along the edges of the jet.

Like the model results presented here, Lagrangian observations of the Gulf Stream using neutrally buoyant floats indicate that, when a strong potential vorticity front is present, there is limited cross-frontal fluid transport (Bower and Lozier 1994). The observations also reveal a wide array of fluid particle trajectories, including pathways that reflect the meandering Eulerian structure of the stream as well as entrainment and detrainment to and from the stream (Bower and Rossby 1989). In an effort to better understand the complicated motion revealed in the observations, results from a dynamical systems analysis similar to that presented here have been utilized to aid the interpretation of a set of Gulf Stream RAFOS trajectories (Lozier et al. 1997). Recognizing that the analysis of the observed Lagrangian motion would be simplified in a moving reference frame, the study of Lozier et al. (1997) provided the first look at float trajectories in a reference frame moving with the phase speed of Gulf Stream meanders to expose the underlying geometrical structure of the observed flow.

The flow we have analyzed is a very idealized model of an oceanic jet such as the Gulf Stream, and the desire to study more complex flows naturally arises. It is our hope that this study will encourage future investigations that will continue to test the extent to which a dynamical systems approach can be effectively applied to physically relevant flows to address mixing and transport issues in the ocean and atmosphere.

REFERENCES

Auer, S. J., 1987: Five-year climatologicial survey of the Gulf Stream System and its associated rings. *J. Geophys. Res.,* **92** (C11), 11 709–11 726..

Behringer, R. P., S. D. Meyers, and H. L. Swinney, 1991: Chaos and mixing in a geostropic flow. *Phys. Fluids A,* **3** (5), 1243–1249..

Bower, A. S., 1991: A simple kinematic mechanism for mixing fluid parcels across a meandering jet. *J. Phys. Oceanogr.,* **21,** 173–180.. Find this article online

——, and T. Rossby, 1989: Evidence of cross-frontal exchange processes in the Gulf Stream based on isopycnal RAFOS float data. *J. Phys. Oceanogr.,* **19,** 1177–1190.. Find this article online

——, and M. S. Lozier, 1994: A closer look at particle exchange in the Gulf Stream. *J. Phys. Oceanogr.,* **24,** 1399–1418.. Find this article

online

Brown, M. G., and R. M. Samelson, 1994: Particle motion in vorticity-conserving, two-dimensional incompressible flows. *Phys. Fluids,* **6** (9), 2875–2876..

Canuto, C., M. Y. Hussaini, A. Quarteroni, and T. A. Zang, 1988: *Spectral Methods in Fluid Dynamics.* Springer-Verlag, 567 pp..

del-Castillo-Negrete, D., and P. J. Morrison, 1993: Chaotic transport of Rossby waves in shear flow. *Phys. Fluids A,* **5** (4), 948–965..

Duan, J., and S. Wiggins, 1996: Fluid exchange across a meandering jet with quasiperiodic variability. *J. Phys. Oceanogr.,* **26,** 1176–1188.. Find this article online

Dutkiewicz, S., A. Griffa, and D. B. Olson, 1993: Particle diffusion in a meandering jet. *J. Geophys. Res.,* **98** (C9), 16 487–16 500..

Flierl, G. R., P. Malanotte-Rizzoli, and N. J. Zabusky, 1987: Nonlinear waves and coherent vortex structures in barotropic *β*-plane jets. *J. Phys. Oceanogr.,* **17,** 1408–1438.. Find this article online

Guckenheimer, J., and P. Holmes, 1983: *Nonlinear Oscillations, Dynamical Systems, and Bifurcations of Vector Fields.* Applied Mathematical Sciences, Vol. 42, Springer-Verlag, 459 pp..

Haller, G., and A. Poje, 1998: Finite time transport in aperiodic flows. *Physica D,* in press..

Lai, D. Y., and P. L. Richardson, 1977: Distribution and movement of Gulf Stream rings. *J. Phys. Oceanogr.,* **7,** 670–683.. Find this article online

Lee, T., and P. Cornillon, 1996: Propagation and growth of Gulf Stream meanders between 75° and 45°W. *J. Phys. Oceanogr.,* **26,** 225–241.. Find this article online

Lozier, M. S., L. J. Pratt, A. M. Rogerson, and P. D. Miller, 1997: Exchange geometry revealed by float trajectories in the Gulf Stream. *J. Phys. Oceanogr.,* **27,** 2327–2341.. Find this article online

Malhotra, N., and S. Wiggins, 1998: Geometric structures, lobe dynamics, and Lagrangian transport in flows with aperiodic time-dependence, with applications to Rossby wave flow. *J. Nonlinear Sci.,* **8** (4), 401–456..

Meyers, S. D., 1994: Cross-frontal mixing in a meandering jet. *J. Phys. Oceanogr.,* **24,** 1641–1646.. Find this article online

Miller, P., C. K. R. T. Jones, G. Haller, and L. Pratt, 1996: Chaotic mixing across oceanic jets. *Chaotic, Fractal, and Nonlinear Signal Processing,* R. Katz, Ed., AIP Conf. Proc. 375, AIP Press, 591–604..

— ,— ,A. M. Rogerson, and L. J. Pratt, 1997: Quantifying transport in numerically generated vector fields. *Physica D,* **110,** 105–122..

Ngan, K., and T. G. Shepherd, 1997: Chaotic mixing and transport in Rossby-wave critical layers. *J. Fluid Mech.,* **334,** 315–351..

Nusse, H. E., and J. Yorke, 1998: *Dynamics: Numerical Explorations.* 2d ed. Applied Mathematical Sciences, Vol. 101, Springer-Verlag, 484 pp..

Ottino, J. M., 1989: *The Kinematics of Mixing: Stretching, Chaos, and Transport.* Cambridge University Press, 364 pp..

Pierrehumbert, R. T., 1991a: Chaotic mixing of tracer and vorticity by modulated travelling Rossby waves. *Geophys. Astrophys. Fluid Dyn.,* **58,** 285–319..

— ,1991b: Large-scale horizontal mixing in planetary atmospheres. *Phys. Fluids A,* **3** (5), 1250–1260..

Polvani, L. M., and J. Wisdom, 1990: Chaotic Lagrangian trajectories around an elliptical vortex patch embedded in a constant and uniform background shear flow. *Phys. Fluids A,* **2** (2), 123–126..

Pratt, L. J., M. S. Lozier, and N. Beliakova, 1995: Parcel trajectories in quasigeostrophic jets: Neutral modes. *J. Phys. Oceanogr.,* **25,** 1451–1466.. Find this article online

Samelson, R. M., 1992: Fluid exchange across a meandering jet. *J. Phys. Oceanogr.,* **22,** 431–440.. Find this article online

Sommeria, J., S. D. Meyers, and H. L. Swinney, 1989: Laboratory model of a planetary eastward jet. *Nature,* **337** (6202), 58–61..

Wiggins, S., 1992: *Chaotic Transport in Dynamical Systems.* Interdisciplinary Applied Mathematics, Vol. 2, Springer-Verlag, 301 pp..

Tables

Table 1. Parameter settings for the three cases analyzed along with the (nondimensional) simulation time t_0 chosen as the initial time for the analysis, the translation speed c of the frame of reference, and the dominant time period T exhibited in the moving reference frame.

Case	(Re, β, k_0)	t_0	c	T
I	$(10^4, 0.103, 0.74)$	650	0.1255	52.5
II	$(10^4, 0.207, 0.98)$	300	0.1641	31.5
III	$(10^3, 0.103, 0.74)$	200	0.1209	56.5

Click on thumbnail for full-sized image.

Table 2. Nondimensional lobe areas for the lobes illustrated in Fig. 9 for case I.

Group A		Group B		Group C		Group D	
Lobe	Area	Lobe	Area	Lobe	Area	Lobe	Area
1	1.143194	2	0.942861	3	0.307037	4	0.713867
5	0.997582	6	0.810276	7	0.284402	8	0.721887
9	0.924829	10	0.983440	11	0.704648	12	1.166643

Click on thumbnail for full-sized image.

Table 3. Lobes participating in the retrograde-to-recirculation ($T \longrightarrow C$) and recirculation-to-retrograde ($C \longrightarrow T$) exchange, the cumulative lobe area, and the corresponding transport over the length of the cycle $\Delta t = t_2 - t_1$, for the flow illustrated in Fig. 9 for case I.

Time interval $[t_1, t_2]$	Participating lobes $T \to C : C \to T$	Total lobe area $A_{T \to C} : A_{C \to T}$	Transport $A_{T \to C}/\Delta t : A_{C \to T}/\Delta t$
[38, 98]	1, 3 : 2, 4	1.451 : 1.657	0.0242 : 0.0276
[98, 156]	5, 7 : 6, 8	1.281 : 1.532	0.0221 : 0.0264
[156, 210]	9, 10 : 10, 12	1.630 : 2.150	0.0302 : 0.0398

Click on thumbnail for full-sized image.

Table 4. Nondimensional lobe areas for the lobes illustrated in Fig. 10 for case II.

Group A		Group B	
Lobe	Area	Lobe	Area
		1	0.819390
2	0.838730	3	0.787710
4	0.182250	5	0.007154
6	0.548278	7	0.854710
8	0.764800	9	0.769599
10	0.719425	11	0.785175
12	0.864622	13	0.721175
14	0.411970	15	0.516083

Click on thumbnail for full-sized image.

Table 5. Lobes participating in the retrograde-to-recirculation ($T \longrightarrow C$) and recirculation-to-retrograde ($C \longrightarrow T$) exchange, the cumulative lobe area, and the corresponding transport over the length of the cycle $\Delta t = t_2 - t_1$, for the flow illustrated in Fig. 10 for case II.

Time interval $[t_1, t_2]$	Participating lobes $T \to C : C \to T$	Total lobe area $A_{T \to C} : A_{C \to T}$	Transport $A_{T \to C}/\Delta t : A_{C \to T}/\Delta t$
[38, 64]	2 : 3	0.839 : 0.788	0.0323 : 0.0303
[64, 96]	4, 6 : 5, 7	0.731 : 0.862	0.0228 : 0.0269
[96, 128]	8 : 9	0.765 : 0.770	0.0239 : 0.0241
[128, 164]	10 : 11	0.719 : 0.785	0.0225 : 0.0245
[164, 196]	12 : 13	0.865 : 0.721	0.0270 : 0.0225
[196, 228]	14 : 15	0.412 : 0.516	0.0129 : 0.0161

Click on thumbnail for full-sized image.

Table 6. Nondimensional lobe areas for the lobes illustrated in Fig. 11 for case III.

Group A		Group B		Group C		Group D	
Lobe	Area	Lobe	Area	Lobe	Area	Lobe	Area
1	1.425146	2	2.023283	3	0.138258	4	0.613037
5	1.011310	6	1.451917	7	0.149030	8	0.464254
9	0.497494	10	0.854587	11	0.2435717		

Click on thumbnail for full-sized image.

Table 7. Lobes participating in the retrograde-to-recirculation ($T \longrightarrow C$) and recirculation-to-retrograde ($C \longrightarrow T$) exchange, the cumulative lobe area, and the corresponding transport over the length of the cycle* $\Delta t = t_2 - t_1$, for the flow illustrated in Fig. 11 for case III.

Table 8. Nondimensional lobe areas for the lobes illustrated in Fig. 12 for case III.

Group A		Group B		Group C		Group D	
Lobe	Area	Lobe	Area	Lobe	Area	Lobe	Area
1	0.189097	2	0.018088	3	0.260920	4	0.121905
5	0.105099	6	0.004102	7	0.365735	8	0.032013

Table 9. Lobes participating in the recirculation-to-jet core ($C \rightarrow J$) and jet core-to-recirculation ($J \rightarrow C$) exchange, the cumulative lobe area, and the corresponding transport over the length of the cycle $\Delta t = t_2 - t_1$, for the flow illustrated in Fig. 12 for case III.

Time interval $[t_1, t_2]$	Participating lobes $C \rightarrow J : J \rightarrow C$	Total lobe area $A_{C \rightarrow J} : A_{J \rightarrow C}$	Transport $A_{C \rightarrow J}/\Delta t : A_{J \rightarrow C}/\Delta t$
[44, 98]	1, 3:2, 4	0.470:0.140	0.0087:0.0026
[98, 154]	5, 7:6, 8	0.471:0.036	0.0084:0.0006

Figures
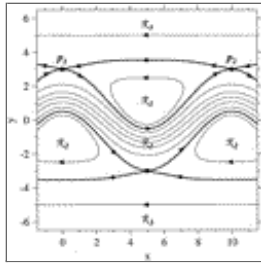
Fig. 1. Streamfunction contours in the moving reference frame for the the kinematic model of the meandering jet from Bower (1991). The bounding streamlines separating the prograde ($\mathcal{R}_1$), recirculation ($\mathcal{R}_2$), and retrograde ($\mathcal{R}_3$) regions are drawn with thick lines. Two hyperbolic points, p_1 and p_2, are indicated.
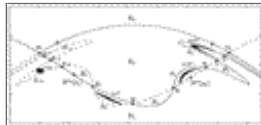
Fig. 2. Poincaré map for the time-periodic meandering jet flow analyzed by Pratt et al. (1995), from Miller et al. (1996), illustrating the chaotic transport between regions $\mathcal{R}_1$ and $\mathcal{R}_2$. Two hyperbolic points, p_1 and p_2, are indicated. Intersections of the stable manifold $W^s(p_2)$ (dashed line) and unstable manifold $W^u(p_1)$ (solid line) define primary intersection points, q_n and $\tilde{q}_n$, and lobes A_n and B_n. The regime boundary is defined in this case as $W^u(p_1, q_0) \cup W^s(q_0, p_2)$. The mapping of a square patch of fluid within lobe A_{-1} to lobes A_0, A_1, and A_2 at subsequent times is illustrated.
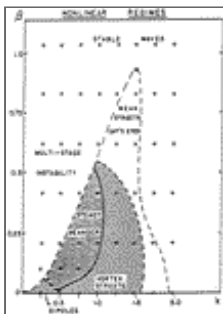
Fig. 3. Nonlinear regime diagram from Flierl et al. (1987) identifying different types of finite-amplitude flow evolution in (β, k_0) phase space for the nonlinear barotropic numerical model.
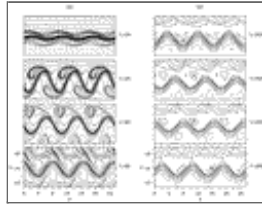
Fig. 4. Evolution of the numerically generated flow as represented by the potential vorticity field for case III. The contour increment is $\Delta q = 0.1$. Only a portion of the computational domain is shown. (a) The early nonlinear evolution of the unstable jet, $t = 20, 40, 60, 80$. (b) The nearly time-periodic meandering jet flow, $t = 200, 220, 240, 260$. A patch of vorticity within a recirculation region is marked with an asterisk.

Fig. 5. Time dependence of the flow in the stationary reference frame for case III. (a) Time series of the meridional velocity, $\mathcal{V}(t)$, in the stationary reference frame for two points, located at $(x, y) = (6.0, 12.8)$ (marked "1") and $(x, y) = (8.0, 15.0)$ (marked "2"). (b) The power spectrum obtained using the maximum entropy method. The spectral peak at $\omega/(2\pi) = 0.0138$ corresponds to the propagation speed of the dominant meander, $c = (L_D/n_0)\,(\omega/(2\pi))$.
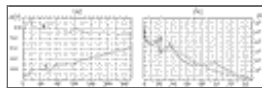
Fig. 6. Time dependence of the flow in the moving reference frame for case III. (a) Time series of the meridional velocity, $\mathcal{V}(t)$, in the moving reference frame for a point located near the jet axis at $(x, y) = (6.0, 12.8)$ (marked "1"), and for a point located in a recirculation region at $(x, y) = (8.0, 15.0)$ (marked "2"). (b) The corresponding power spectrum. The spectral peaks in the range $\omega/(2\pi) = (0.017, 0.018)$ are associated with the nutation period.
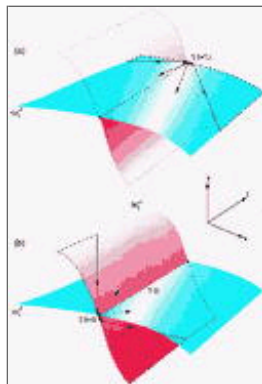
Fig. 7. Schematic of the computational approach used to approximate the finite-time material surfaces and the hyperbolic trajectory $\gamma(t)$. (a) The stable surface, $\mathcal{W}^{s}_{\gamma}$ (shown in blue), is generated by trajectories that exponentially move away from the hyperbolic region in the vicinity of $\gamma(t = T_f)$ as time regresses; (b) the unstable surface, $\mathcal{W}^{u}_{\gamma}$ (shown in red), is generated by trajectories that exponentially move away from $\gamma(t = 0)$ as time progresses. Portions of $\mathcal{W}^{s}_{\gamma}$ [in (a)] and $\mathcal{W}^{u}_{\gamma}$ [in (b)] outlined with the dotted line are not computed but are included in the figure to aid the visualization of the surfaces.

Fig. 8. (a) Schematic of the time evolution of the surfaces $\mathcal{W}^s_{\gamma_1}$ (shown in blue) and $\mathcal{W}^u_{\gamma_2}$ (shown in red) for two distinguished hyperbolic trajectories, $\gamma_1(t)$ and $\gamma_2(t)$, on the northern side of the jet. Also shown are portions of $\mathcal{W}^u_{\gamma_1}$ (shown in orange) and $\mathcal{W}^s_{\gamma_2}$ (shown in purple). The intersection point used to define the regime boundary, depicted as point q_0 at early times and q_{-1} at later times, is shown in black. Two lobes, **A** and **B**, are also marked. (b) Time slices of the tangling stable and unstable surfaces near the intersection point q_0, illustrating how the regime boundary deforms and is redefined. Segments of the stable (shown in blue) and unstable (shown in red) curves are used to define the regime boundary which is indicated by the thick line style. At time t_0, the boundary is $W^s_{\gamma_1,t}[\gamma_1, q_0] \cup W^u_{\gamma_2,t}[q_0, \gamma_2]$. At time $t > t_0$, the boundary has deformed, but is still defined with respect to the intersection point q_0. At time t_1, the boundary is redefined in terms of the intersection point q_{-1}, and lobes A and B are thereby "transported" to different flow regimes resulting in a fluid exchange.
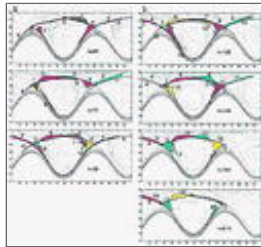
Fig. 9. Results of the aperiodic analysis for case I corresponding to (Re, β, k_0) = $(10^4, 0.103, 0.74)$.
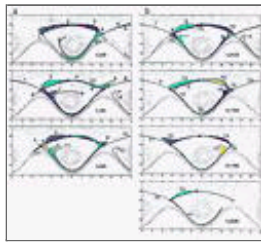
Fig. 10. Results of the aperiodic analysis for case II corresponding to (Re, β, k_0) = $(10^4, 0.207, 0.98)$.
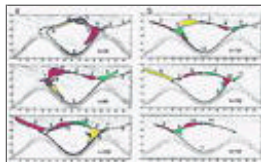
Fig. 11. Results of the aperiodic analysis for case III corresponding to (Re, β, k_0) = $(10^3, 0.103, 0.74)$.
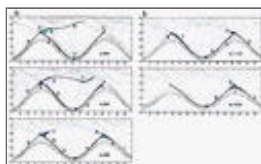
Fig. 12. Results of the aperiodic analysis depicting the jet core–recirculation exchange for case III.
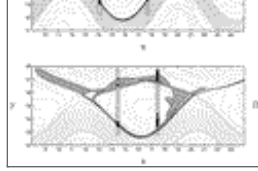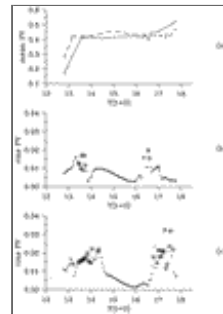
Click on thumbnail for full-sized image.

Fig. 13. Composite illustrations of the potential vorticity field (contoured in the dotted line style), lobe structure (shaded), and two meridional transects through the cat's eye region where Lagragian particles are initially positioned 0.05 units apart for (a) case I at time $t = 98$, and (b) case III at time $t = 102$. A total of 242 [202] particles for (a) [(b)] are tracked for 200 time units. The initial positions of particles that exhibit rapid potential vorticity transitions, $\Delta q > 0.01$ [$\Delta q > 0.015$] for (a) [(b)] over any 10-unit time interval, are plotted with an asterisk (see also Figs. 14 ⊙ and 15 ⊙).
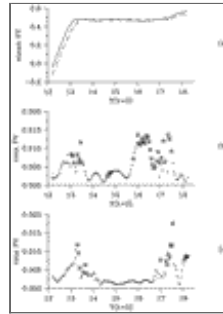
Click on thumbnail for full-sized image.

Fig. 14. Lagrangian potential vorticity statistics for case I. (a) Mean potential vorticity vs initial meridional location, $Y(t = 0)$, for the western transect (plotted with the solid line) and eastern transect (plotted with the dashed line) shown in Fig. 13a ⊙. (b) Standard deviation vs initial meridional location for the western transect. Particle trajectories that exhibit rapid potential vorticity transitions ($\Delta q > 0.01$ over 10 time units) have their rms data point augmented with a square. (c) As in (b) but for the eastern transect.

Click on thumbnail for full-sized image.

Fig. 15. Lagrangian potential vorticity statistics for case III. (a) Mean potential vorticity vs initial meridional location, $Y(t = 0)$, for the western transect (plotted with the solid line) and eastern transect (plotted with the dashed line) shown in Fig. 13b ⊙. (b) Standard deviation vs initial meridional location for the western transect. Particle trajectories that exhibit rapid potential vorticity transitions ($\Delta q > 0.015$ over 10 time units) have their rms data point augmented with a square. (c) As in (b) but for the eastern transect.

Corresponding author address: Dr. A. M. Rogerson, MS #21, Room 304A, Woods Hole Oceanographic Institution, Woods Hole, MA 02543-1541.

E-mail: arogerson@whoi.edu